Dalton Transactions

ROYAL SOCIETY OF CHEMISTRY

PAPER

View Article Online
View Journal | View Issue

Cite this: *Dalton Trans.*, 2023, **52**, 17514

A new high-pressure polymorph of $K_2MoO_2F_4$†

Fabian Zimmerhofer and Hubert Huppertz *

Received 13th September 2023,
Accepted 3rd November 2023

DOI: 10.1039/d3dt02992a

rsc.li/dalton

In this paper, a new high-pressure (HP) polymorph of the otherwise known oxyfluoride $K_2MoO_2F_4$ is presented. The crystal structure was determined by use of single-crystal X-ray diffractometry and its features are described in detail herein. HP-$K_2MoO_2F_4$ crystallizes in the monoclinic space group $C2/m$ (no. 12) with the cell parameters a = 13.8579(5), b = 5.8109(2), c = 6.9442(3) Å, β = 90.36(1)°, V = 559.18(4) Å^3, and Z = 4 at T = 301(2) K. Bond valence (BV) and charge distribution (CHARDI) calculations were carried out to support the assignment of oxygen and fluorine to the various anion positions and Madelung part of lattice energy (MAPLE) calculations were used to validate the structure model. Infrared spectroscopy provided further information on the structure and water content of the inseparable side phase.

Introduction

Oxyfluorides as a substance class exhibit a wide variety of different structural motifs, owed in no small part to the simultaneous presence of both fluorine and oxygen as anions.[1] Even seemingly small changes in the structure of an oxyfluoride can have a great impact on its physical and electronic properties.[2] High-pressure synthesis allows for the discovery of unusually strained, distorted and even completely novel structural motifs, whose formation can only be observed when subjected to the most extreme conditions, making it a powerful tool in the search for new functional materials.

Oxyfluorides are of general scientific and industrial interest when it comes to applications as transparent glass ceramics,[3] nonlinear optical materials,[4] deep red-emitting Mn^{4+}-activated phosphors,[5] and in next-generation batteries.[6,7] Oxyfluorides of the type $A_2BO_2F_4$ (A = Na, K, Rb or Cs and B = Mo or W) are particularly well known for their luminescence properties upon doping with Mn^{4+}. While most combinations have already been described in the literature and successfully doped with Mn^{4+} to yield a red luminescent material, variants containing solely K seem to be more intricate.[8–15] Even though both $K_2MoO_2F_4$ as well as $K_2WO_2F_4$ have been mentioned before in the literature, there have been no reports of successful doping with Mn^{4+}.[16,17]

As an immediate relative of the title compound, the existence of the monohydrate $K_2MoO_2F_4{\cdot}H_2O$ was first reported in 1954[18] and its properties investigated extensively in the mid-1960s in a series of papers by Grandjean and Weiss.[19–22] The monohydrate compound crystallizes in the monoclinic crystal system in space group $P2_1/c$ (no. 14) with the lattice parameters a = 6.214, b = 6.192, c = 18.079 Å and β = 96.27°.[22] The crystal structure is made up of isolated $[MoO_2F_4]^{2-}$ octahedra with oxygen atoms occupying *cis* positions. The water molecule acts as a bridge between two individual octahedra by bonding to the oxygen atom of one octahedron and to the fluorine atom of another. With O–H_2O distances of 3.10 Å and a frequency of 3620 cm^{-1} for the O–H stretching vibration in the IR spectrum, the hydrogen bonding is reported to be quite weak.[19]

The anhydrous compound $K_2MoO_2F_4$ was discovered fourteen years later in 1968 by Pinsker and Kuznetsov, who determined its crystal structure by electron diffraction experiments.[17] It crystallizes in the tetragonal space group $P4/nmm$ (no. 129) with the lattice parameters a = 6.19 and c = 8.81 Å and ordered O and F atoms. In the anhydrous variant, the oxygen atoms are in *trans* position with one Mo–O bond shorter than the other, leading to a displacement of the Mo atom from the equatorial plane by about 0.17 Å.[17]

Decades later in 1992 and 1993, the luminescence properties of both variants were investigated under long wavelength UV excitation at a temperature of 4.2 K, revealing a broad and structureless emission band at ≈680 nm stemming from charge-transfer transitions.[23,24] Since then, no additional information on $K_2MoO_2F_4$ and its hydrates has been published.

In this paper, we present the high-pressure/high-temperature synthesis and crystal structure elucidation of a new polymorph of anhydrous $K_2MoO_2F_4$ exhibiting mixed O|F occupancy.

Results and discussion

HP-$K_2MoO_2F_4$ was synthesized under high-pressure/high-temperature conditions at 3.0 GPa and 800 °C using a

University of Innsbruck, Institute of General, Inorganic and Theoretical Chemistry, Innrain 80-82, 6020 Innsbruck, Austria. E-mail: Hubert.Huppertz@uibk.ac.at

†Electronic supplementary information (ESI) available. CCDC 2294711. For ESI and crystallographic data in CIF or other electronic format see DOI: https://doi.org/10.1039/d3dt02992a

2 : 1 mixture of KHF_2 and MoO_3. For a detailed description of the synthetic procedure, refer to the Experimental section.

The crystal structure of high-pressure $K_2MoO_2F_4$

HP-$K_2MoO_2F_4$ crystallizes in the monoclinic space group $C2/m$ (no. 12) with the cell parameters a = 13.8579(5), b = 5.8109(2), c = 6.9442(3) Å, β = 90.36(1)°, V = 559.18(4) Å^3, and Z = 4, at T = 301(2) K. An overview of the crystal data and structure refinement process is given in Table 1. Wyckoff positions, atomic coordinates, equivalent isotropic displacement parameters, and occupancies are listed in Table 2. Anisotropic displacement parameters as well as a selection of interatomic distances are reported in Tables 3 and 4, respectively.

Table 1 Crystal data and structure refinement of HP-$K_2MoO_2F_4$ (standard deviations in parentheses)

Empirical formula	$K_2MoO_2F_4$
Molar mass/g mol^{-1}	282.14
Crystal system	Monoclinic
Space group	$C2/m$ (no. 12)
Single-crystal diffractometer	Bruker D8 Quest Kappa
Radiation; wavelength λ/pm	MoKα; 71.073
a/Å	13.8579(5)
b/Å	5.8109(2)
c/Å	6.9442(3)
β/°	90.36(1)
V/Å^3	559.18(4)
Formula units per cell Z	4
Calculated density/g cm^{-3}	3.351
Crystal size/mm^3	0.10 × 0.05 × 0.02
Temperature/K	301(2)
Absorption coefficient/mm^{-1}	3.842
F(000)/e	528
2θ range for data collection/°	5.9–75.00
Range in hkl	$-23 \le h \le 23$ $-9 \le k \le 9$ $-11 \le l \le 11$
Total no. of reflections	9484
Independent reflections	1568
R_{int}	0.0365
Reflections with $I \ge 2\sigma(I)$	1493
Data; restraints; parameters	1568; 0; 51
Absorption correction	Multiscan
Final R_1; wR_2 [$I > 2\sigma(I)$]	0.0345; 0.0839
Final R_1; wR_2 (all data)	0.0368; 0.0868
Goodness-of-fit on F^2	1.098
Largest diff. peak; hole/e Å^{-3}	2.83; −2.08
BASF	0.0587(11)

Table 2 Wyckoff positions, atomic coordinates, equivalent isotropic displacement parameters U_{eq} (Å^2), and occupancies for HP-$K_2MoO_2F_4$ (standard deviations in parentheses)

Atom	Wyckoff position	x	y	z	U_{eq}	*occ.*
Mo1	4*i*	0.39122(2)	0	0.22990(4)	0.0225(2)	1
K1	4*i*	0.05850(6)	0	0.2590(2)	0.0268(2)	1
K2	4*i*	0.26774(6)	0	0.7156(2)	0.0316(2)	1
F1	8*j*	0.3734(2)	0.2341(4)	0.0575(3)	0.0341(4)	$\frac{1}{2}$
O1	8*j*	0.3734(2)	0.2341(4)	0.0575(3)	0.0341(4)	$\frac{1}{2}$
F2	4*i*	0.2478(2)	0	0.2745(4)	0.0352(5)	1
O2	4*i*	0.5165(2)	0	0.2389(5)	0.0304(5)	1
F3	8*j*	0.3850(2)	0.2347(3)	0.4377(2)	0.0299(3)	1

Table 3 Anisotropic displacement parameters U_{ij} (Å^2) for HP-$K_2MoO_2F_4$ (standard deviations in parentheses)

Atom	U_{11}	U_{22}	U_{33}	U_{23}	U_{13}	U_{12}
Mo1	0.0228(2)	0.0207(2)	0.0242(2)	0	0.0067(9)	0
K1	0.0285(3)	0.0250(3)	0.0269(3)	0	−0.0019(2)	0
K2	0.0279(3)	0.0246(3)	0.0422(4)	0	0.0023(3)	0
F1|O1	0.049(2)	0.0269(8)	0.0268(8)	0.0095(7)	0.0071(7)	0.0075(7)
F2	0.0160(8)	0.044(2)	0.046(2)	0	0.0013(9)	0
O2	0.0191(9)	0.036(2)	0.037(2)	0	0.0036(9)	0
F3	0.0384(8)	0.0241(7)	0.0273(7)	−0.0099(6)	−0.0023(6)	0.0033(6)

Table 4 Selected interatomic distances (Å) in HP-$K_2MoO_2F_4$ (standard deviations in parentheses)

Atoms	Distance	Atoms	Distance	Atoms	Distance
Mo1–F1|O1	1.828(2) 2×	K1–F1|O1a	2.852(2) 2×	K2–F1|O1a	2.955(2) 2×
Mo1–F2	2.013(2)	K1–F1|O1b	3.299(2) 2×	K2–F1|O1b	3.097(2) 2×
Mo1–O2	1.737(3)	K1–F2	2.625(2)	K2–F2a	2.9143(2) 2×
Mo1–F3	1.988(2) 2×	K1–O2	2.9663(6) 2×	K2–F2b	3.073(3)
∅	**1.897**	K1–F3a	2.721(2) 2×	K2–O2	3.005(3)
		K1–F3b	3.120(2) 2×	K2–F3a	2.822(2) 2×
		∅	**2.958**	K2–F3b	2.875(2) 2×
				∅	**2.950**

Like the monohydrate compound, the crystal structure of HP-$K_2MoO_2F_4$ is composed of isolated $[MoO_2F_4]^{2-}$ octahedra embedded in a matrix of potassium atoms. While O and F atoms are ordered for both the normal-pressure (NP) modification and the monohydrate, HP-$K_2MoO_2F_4$ contains a single mixed-anion position occupied equally by F and O (see Fig. 1). This particularity has no effect on the average composition of the octahedron but indicates the possible existence of $[MoO_3F_3]^{3-}$ and $[MoOF_5]^{-}$ building blocks within the crystal structure. Each Mo atom is bonded to three F atoms, an O atom and two mixed O|F positions. The bond lengths range from about 2.00 Å for Mo–F to 1.83 Å for Mo–O|F and 1.74 Å for Mo–O, illustrating the more covalent bonding character of the Mo–O bond in comparison to the Mo–F bond (see Fig. 2). This discrepancy in the bonding characteristics of oxygen and fluorine also serves as the basis for the distinction between them using the bond valence (BV) and charge distribution (CHARDI) concepts (see chapter BV, CHARDI, and MAPLE calculations).

In addition to the sole Mo position, two crystallographically independent potassium positions are present in HP-$K_2MoO_2F_4$. K1 is elevenfold coordinated by five fluorine, two oxygen, and four mixed-anion positions in a manner resembling an anticuboctahedron, missing one anion contact due to connection to a second K2 polyhedron *via* a shared face (see Fig. 3). K2, on the other hand, is fully anticuboctahedrally coordinated by seven fluorine, four mixed-anion, and a single oxygen position. Bond distances in the K1 polyhedron vary heavily in length from 2.625(2) to 3.299(2) Å due to a large degree of distortion. The more symmetrical anticuboctahedral coordination sphere of K2 allows for a more even distribution of bond lengths ranging from 2.822(2) to 3.097(2) Å (see Table 4).

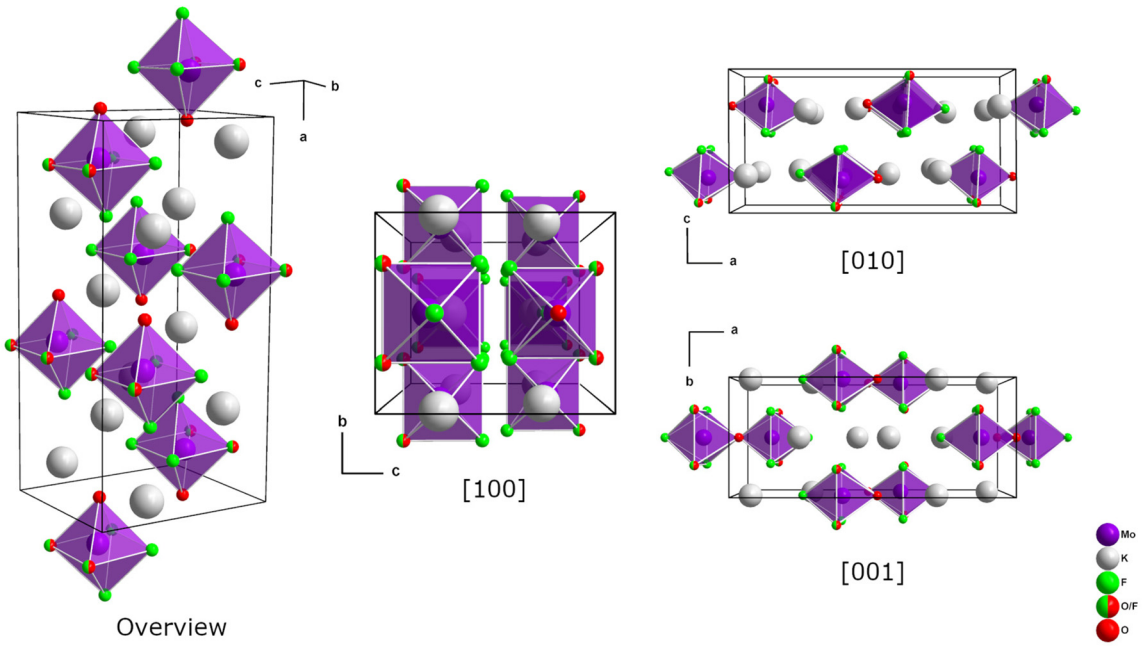

Fig. 1 The crystal structure of HP-$K_2MoO_2F_4$.

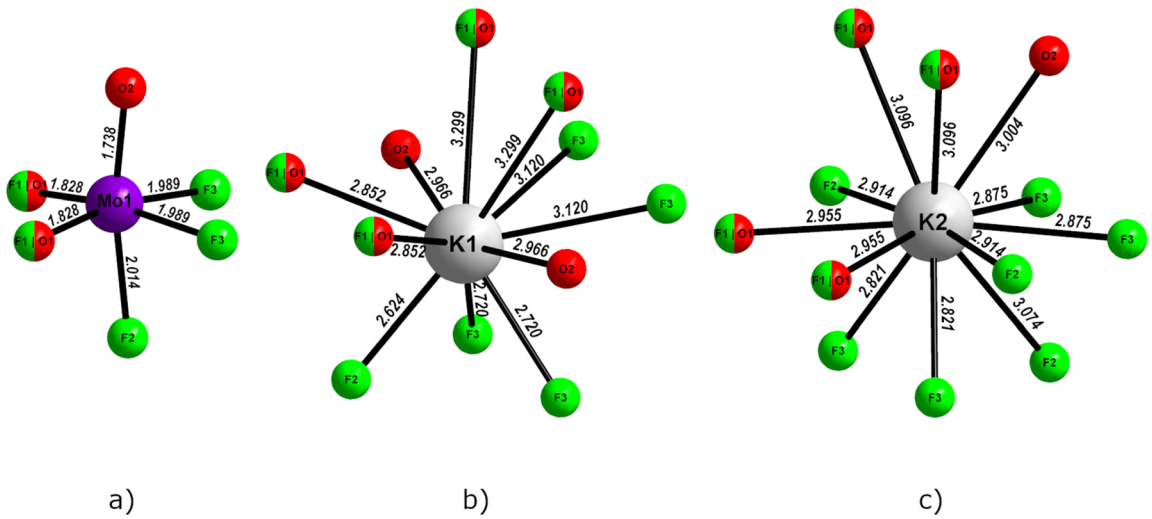

Fig. 2 Coordination sphere of (a) Mo1, (b) K1, and (c) K2. Bond distances are given in Å.

A thorough database search revealed the existence of a remarkably similar yet different structure in $(NH_4)_2NbOF_5$. Although all the main structural motifs are identical to those of the title compound, the $[NbOF_5]^{2-}$ octahedra's orientation in the unit cell is slightly different. Because of this discrepancy, a mirror plane perpendicular to *b* as well as the inversion center are lost, reducing the symmetry of $(NH_4)_2NbOF_5$ down to space group *C*2 (see Fig. 4). Searches for structures with higher symmetry from which the herein described atom arrangements could be derived, were unsuccessful. While there is no shortage of octahedrally coordinated transition metals cations and anticuboctahedrally coordinated alkali metal cations, it is the heavily distorted elevenfold coordination of K1 and the interconnectivity of the polyhedra mimicking an anticuboctahedral environment that make this structure unique.

Powder X-ray diffraction and phase stability

Despite numerous attempts at synthesis including variances in starting materials, stoichiometry, pressure and temperature, we were unable to synthesize HP-$K_2MoO_2F_4$ phase-pure as of yet. Regardless of the exact reaction conditions, a successful synthesis of HP-$K_2MoO_2F_4$ always came hand in hand with the formation of some amount of its hydrate $K_2MoO_2F_4{\cdot}H_2O$ as a

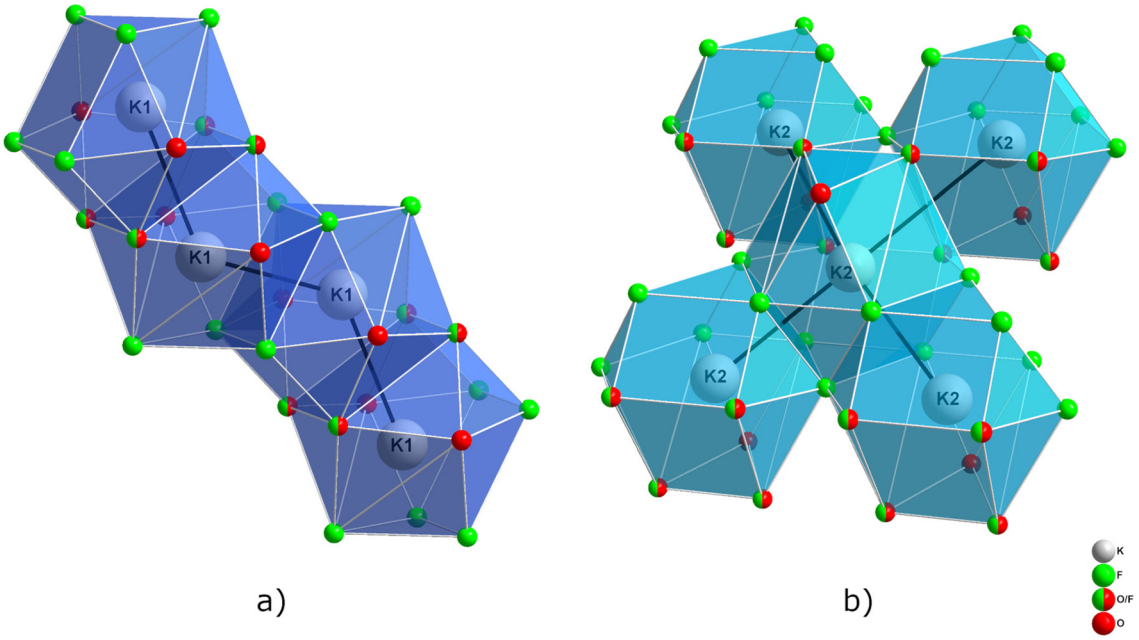

Fig. 3 (a) Connection of K1 polyhedra illustrating the heavily distorted elevenfold 'anticuboctahedron-like' coordination. (b) Connection of K2 anticuboctahedral coordination polyhedra.

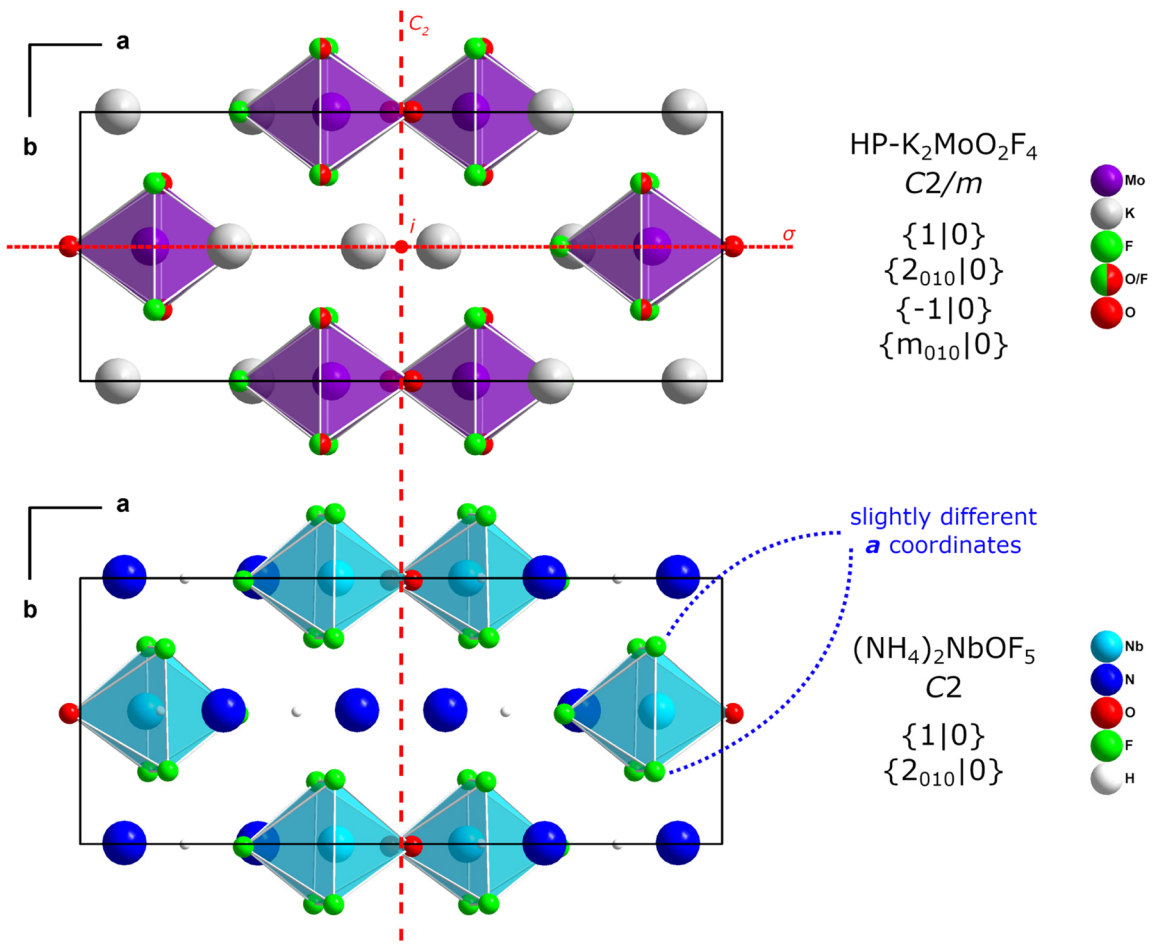

Fig. 4 Comparison between the crystal structures of HP-$K_2MoO_2F_4$ (top) and $(NH_4)_2NbOF_5$ (bottom). Seitz symbols of all possible non-translational symmetry operations are depicted on the right-hand side. C_2: rotation axis of order 2; σ: mirror plane, i: inversion center.

side phase. Recorded reflection positions for both HP-$K_2MoO_2F_4$ as well as $K_2MoO_2F_4{\cdot}H_2O$ agreed well with the ones calculated from the single-crystal structure solutions. Since measured intensities for some reflections deviated quite significantly from expected values, preferred crystallite orientation had to be taken into account for the Rietveld refinement in Fig. 5. The composition of the product mixture was calculated to be ≈83% HP-$K_2MoO_2F_4$ and ≈17% $K_2MoO_2F_4{\cdot}H_2O$, although a small amount of unidentified side phases is present as well. Additional information on the Rietveld refinement can be found in the ESI.†

The high-pressure modification of $K_2MoO_2F_4$ does not appear to be stable at ambient conditions for extended periods of time. When exposed to air, a gradual conversion to the hydrate $K_2MoO_2F_4{\cdot}H_2O$ can be observed. The degradation starts off rather fast but slows down considerably once a certain concentration is reached. This phenomenon is most likely caused by the formation of a passivation layer on the particle surfaces, protecting inner layers from further contact with water. When the passivation layer is disturbed by homogenization of the sample, a significant increase in concentration of the hydrate can be observed the following day. Moreover, the first clear signs of formation of an additional unidentified side phase, whose concentration continues to increase upon further exposition to air, begin to show. An evolution of the phase composition upon exposition to air is illustrated in Fig. 6.

When submerged in water, HP-$K_2MoO_2F_4$ instantly decomposes, indicated by a sudden change in color from light grey to black. Identification of the hydrolysis products *via* PXRD proved difficult due to their amorphous nature, but the formation of some sort of potassium molybdenum (hydr)oxide seems to be the most likely outcome.

Doping attempts of HP-$K_2MoO_2F_4$ with Mn^{4+}

As mentioned in the introduction, oxyfluorides of the type $A_2BO_2F_4$ (A = Na, K, Rb or Cs and B = Mo or W) are particularly well known for their deep-red luminescence upon doping with Mn^{4+}. However, neither direct doping of HP-$K_2MoO_2F_4$ *via* addition of K_2MnF_6 or MnO_2 to the starting materials nor mechanical doping *via* ball mill in a secondary step after synthesis have been successful. While attempts at direct doping lead to the formation of additional unknown side phases, mechanical ball milling actively facilitates the transformation of HP-$K_2MoO_2F_4$ into the hydrate as well as additional unknown phases. The outcome of a ball milling experiment is heavily dependent on the rotational speed (rpm, revolutions per minute) of the mill as well as the length of pauses between milling cycles. For low rpm experiments with long pauses, traces of intact dopants can still be found in the phase mixture upon completion. When milled for 6 × 10 minutes at 300 rpm with 15 min long pauses, temperatures reach levels high enough for HP-$K_2MoO_2F_4$ to start decomposing. While we have no way of directly measuring the temperature inside the ball mill during the procedure, measurements immediately afterwards indicate that a temperature of 50 °C was likely not exceeded. These observations illustrate the title compound's sensitivity to even slight increases in temperature and its readiness to convert into thermodynamically more stable phases given the chance. It should be noted that complete absence of air and moisture could not be guaranteed for the ball milling procedure, possibly explaining why the hydrate is a major decomposition product. Nevertheless, with a significant amount of HP-$K_2MoO_2F_4$ intact after either method of doping, red luminescence stemming from successfully incorporated Mn^{4+} ions should have been easily identified, ultimately

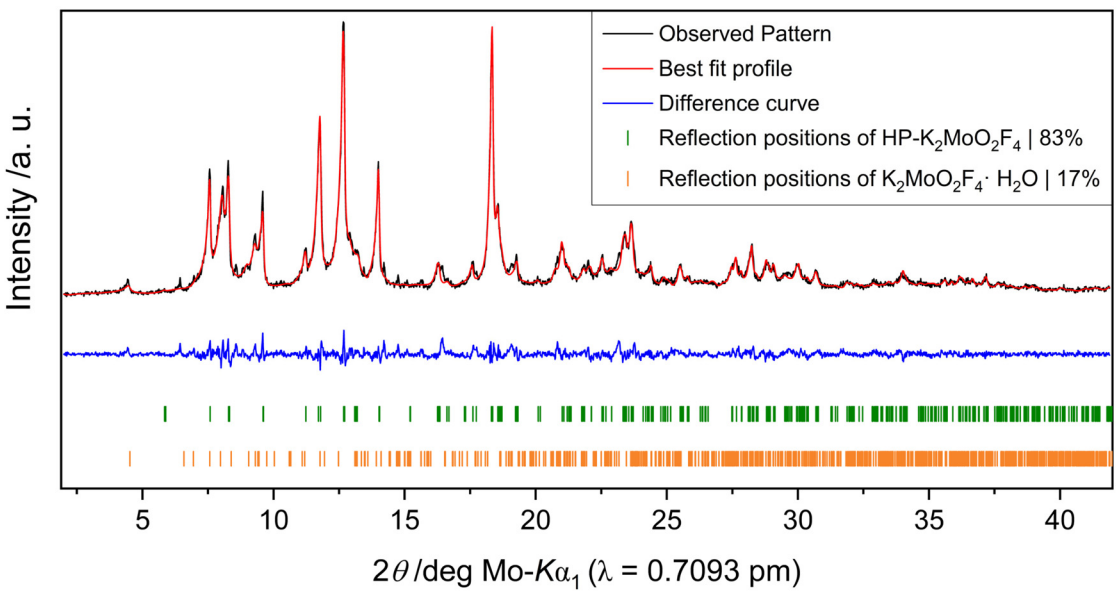

Fig. 5 Rietveld plot of the product mixture. The observed pattern is plotted in black, the best fit profile in red and the difference curve in blue. Reflection positions of HP-$K_2MoO_2F_4$ and $K_2MoO_2F_4{\cdot}H_2O$ are marked in green and orange, respectively.

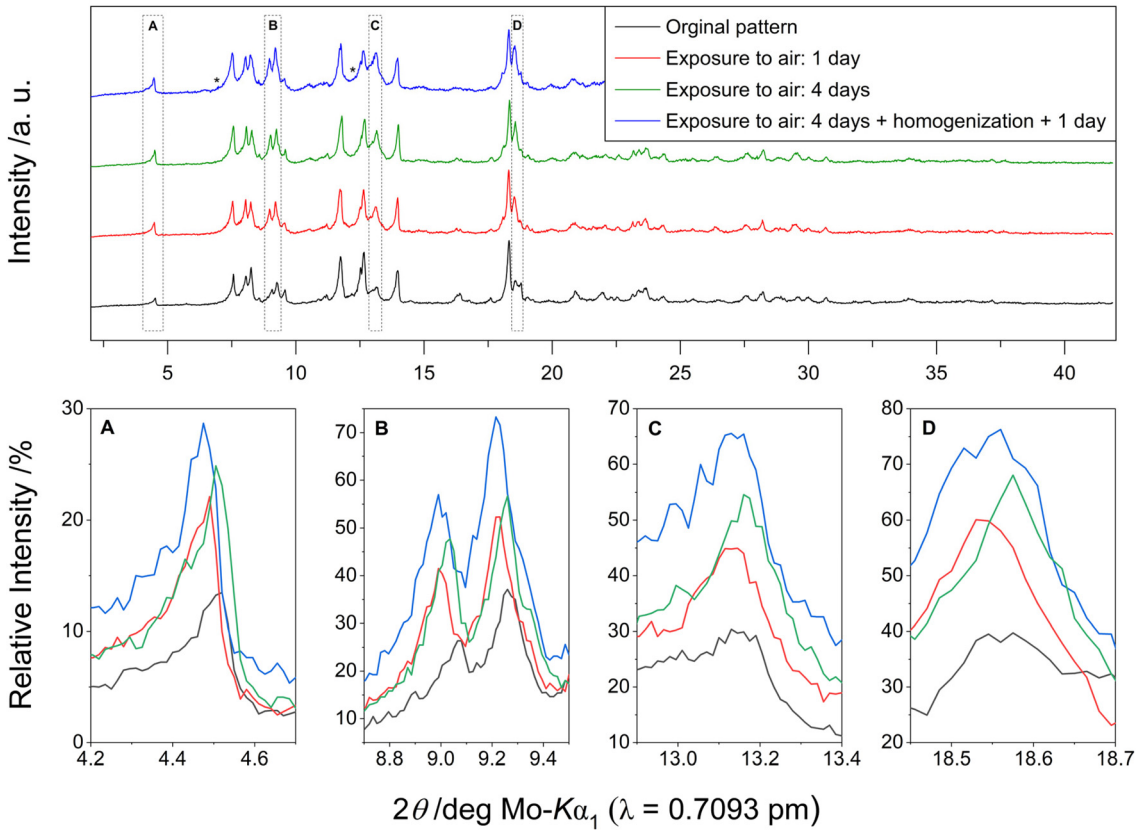

Fig. 6 Evolution of phase composition of the product mixture upon exposition to air. Conversion to the hydrate starts off rather fast (red line) but quickly reaches a plateau due to the formation of a passivation layer (green line). Subsequent homogenization disturbs the outer hydrate layer, allowing more of the high-pressure polymorph to be converted in shorter time (blue line). Asterisks denote reflection positions belonging to a second unidentified side phase, whose presence first becomes clear in the blue data set. A–D illustrate the changes over time by looking at the most prominent reflections of $K_2MoO_2F_4{\cdot}H_2O$. The experiment was carried out in September 2023 in Innsbruck, Austria in an air-conditioned lab at a temperature of 22.5 °C and an average relative humidity of approx. 50%.

leading us to conclude that HP-$K_2MoO_2F_4$ is not a suitable host material for Mn^{4+}.

BV, CHARDI, and MAPLE calculations

Due to how close fluorine and oxygen are to each other on the periodic table, distinction between them based solely on observed electron density often proves quite difficult. In select cases such as this one, site occupation factors during structure refinement can provide a good indication for the distribution of anions over specific crystallographic positions. However, their informative value strongly depends on the nuances of each individual crystal structure, as even the slightest imbalance can render fluorine and oxygen virtually indistinguishable from each other in this way. Aside from expensive and experimentally demanding neutron diffraction experiments, the most reliable yet easily accessible way of differentiating between oxygen and fluorine is a thorough analysis of the bonding situation around each atom *via* bond valence (BV)[25–27] and charge distribution (CHARDI)[28–30] calculations. Both BV and CHARDI are based on Linus Pauling's concept of bond length/bond strength and Rudolf Hoppe's theory of effective coordination numbers (ECoNs).[31–34] Using a series of mathematical equations, oxidation states of atoms in inorganic crystal structures can be estimated based on the chemical identity of the atoms within a coordination polyhedron and the distance between them. The term bond valence was first introduced by Donnay and Allmann in 1970[35] and the concept further expanded upon by Brown *et al.* in the following years.[36,37] While the BV concept relies on the use of empirically determined parameters for its calculations,[38,39] CHARDI is able to avoid the use of such 'standard' values altogether by adopting a Madelung-type (point-charge) description of crystal structures, exclusively incorporating real observed distances into its calculations.[40] The final results of the theoretical calculations agree well with the assignment based on crystallographic data across the board and are reported in Table 5.

The Madelung part of lattice energy (MAPLE) can be used for the validation of structure models.[41–44] If MAPLE values are calculated for the title compound HP-$K_2MoO_2F_4$, then for a well-determined crystal structure this value should agree with the sum of the MAPLE values of the theoretical components KF and MoO_2F_2 within 1%. Using the program Maple v4,[45] the values for HP-$K_2MoO_2F_4$, KF (high-pressure modification) and MoO_2F_2 were calculated and compared. A difference in the

Table 5 Oxidation states of atoms in HP-$K_2MoO_2F_4$ calculated *via* the BV ($\sum V$) and CHARDI ($\sum Q$) concepts

	Mo1	K1	K2	F1|O1	F2	O2	F3
$\sum V$	+5.59	+1.07	+1.01	−1.40	−0.98	−1.89	−1.00
$\sum Q$	+6.03	+0.99	+0.98	−1.52	−1.00	−1.84	−1.06
Average	+5.81	+1.04	+1.00	−1.46	−0.99	−1.87	−1.03
Theoretical charge	+6.00	+1.00	+1.00	−1.50	−1.00	−2.00	−1.00

respective values of only 0.52% (see Table 6) distinctly indicates a plausible structure model.

Infrared spectroscopy

The most prominent bands in the IR spectrum (see Fig. 7) stem from stretching modes involving the central octahedrally coordinated Mo atom and its bonding partners O and F. Mo–F stretching modes are situated between 400 and 560 cm^{-1}, with the signal at 552 cm^{-1} most likely corresponding to the asymmetric stretching mode. Mo–O vibrational modes are located at slightly higher energies in the spectral region ranging from 900 to 1000 cm^{-1}. The broad absorption bands with local maxima at 3441 and 3639 cm^{-1} can be attributed to asymmetric and symmetric O–H stretching vibrations, whereas the more defined bands at ≈1621 cm^{-1} can be assigned to the H–O–H bending vibration of the water molecule contained within the side phase $K_2MoO_2F_4{\cdot}H_2O$.

Since the presence of water of crystallization in the "classic" sense, *i.e.* entire water molecules incorporated into the crystalline framework, like is the case for $K_2MoO_2F_4{\cdot}H_2O$, can be ruled out with certainty for HP-$K_2MoO_2F_4$ based on the single-crystal data collected, we are led to believe that the bands related to O–H vibrations in Fig. 7 originate entirely from the

Table 6 Comparison between the calculated MAPLE values for HP-$K_2MoO_2F_4$ and the corresponding theoretical starting materials KF (high-pressure modification) and MoO_2F_2 according to the equation: 2 KF + MoO_2F_2 → $K_2MoO_2F_4$

KF (HP),[46] kJ mol^{-1}	924 (×2)
MoO_2F_2,[47] kJ mol^{-1}	22 864
$\sum$ of starting materials, kJ mol^{-1}	24 712
HP-$K_2MoO_2F_4$, kJ mol^{-1}	24 584
Difference, kJ mol^{-1}	128
Difference in %	**0.52**

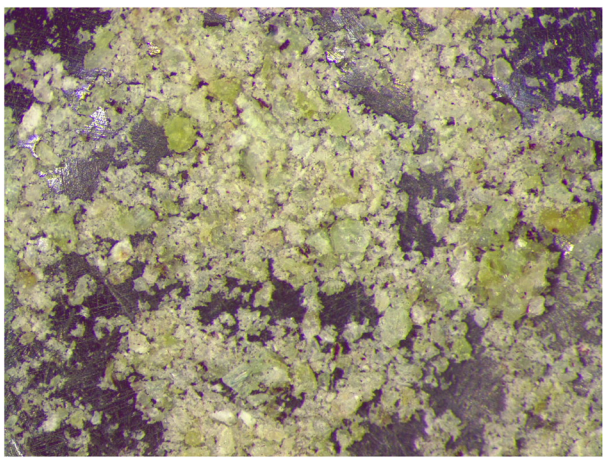

Fig. 8 Photograph of the recovered product under an optical microscope.

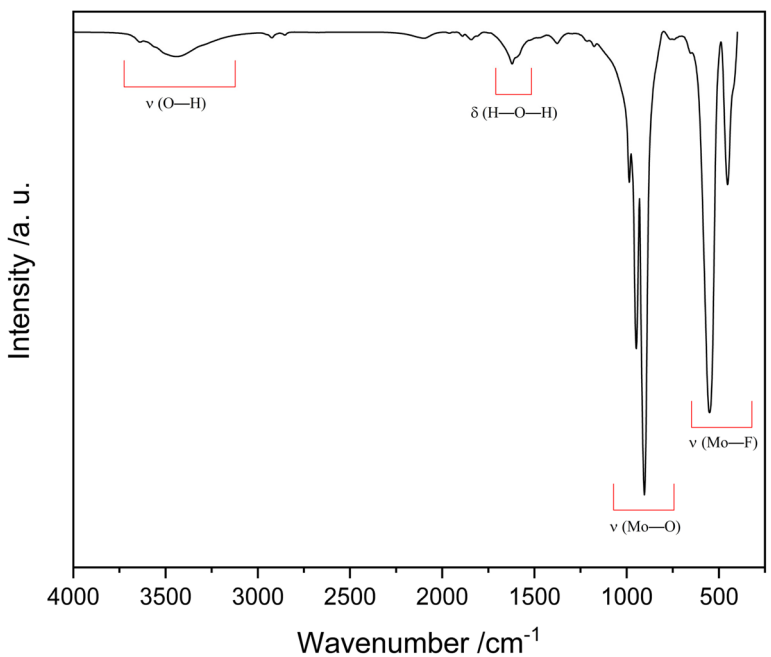

Fig. 7 Infrared spectrum of the powdered product mixture containing HP-$K_2MoO_2F_4$ and $K_2MoO_2F_4{\cdot}H_2O$. The bands were assigned by comparison to similar compounds reported in literature.[48,49] *ν*: stretching vibration, *δ*: bending vibration.

side phase. However, since the high-pressure polymorph cannot be separated from the hydrate side phase and is itself highly susceptible to air and water, conclusive analytical proof for the absence of H atoms is difficult to obtain. As a result, even though we do not believe this to be the case given the data, we cannot completely rule out the possibility of a certain amount of OH groups being present in the new high-pressure phase.

Conclusion

A new high-pressure modification of the oxyfluoride compound $K_2MoO_2F_4$ was obtained using a multianvil setup and characterized *via* single-crystal X-ray diffractometry. It crystallizes in the monoclinic crystal system in space group *C*2/*m* (no. 12) with the cell parameters a = 13.8579(5), b = 5.8109(2), c = 6.9442(3) Å, β = 90.36(1)°, V = 559.18(4) Å^3, and Z = 4 at T = 301(2) K. The main motif are isolated $[MoO_2F_4]^{2-}$ octahedra embedded in a matrix of potassium atoms, although their exact composition can vary from $[MoO_3F_3]^{3-}$ to $[MoOF_5]^-$ depending on occupation of the mixed-anion site. Said site was identified by analysis of the local bonding environment *via* BV and CHARDI calculations, allowing for a clear assignment of fluorine and oxygen to each individual anion position. MAPLE calculations were carried out to further support the structure model and IR measurements confirmed the presence of water of crystallization within the inseparable side phase. Even though we were unable to conclusively prove the absence of H atoms in the high-pressure polymorph reported in this paper given the circumstances, we believe that cumulative data points toward it being free of water and hydroxy groups. Despite the prevalence of oxyfluorides of the type $A_2BO_2F_4$ (A = Na, K, Rb, or Cs and B = Mo or W) in recent research on deep-red emitting Mn^{4+}-activated red phosphor materials, HP-$K_2MoO_2F_4$ could not be successfully doped with Mn^{4+}.

Experimental section

Synthetic procedure

HP-$K_2MoO_2F_4$ was synthesized under high-pressure/high-temperature conditions in a 1000 t frame press (Max Voggenreiter GmbH, Mainleus, Germany) employing a multi-anvil setup to simulate quasi-hydrostatic pressure conditions. 40.00 mg (0.5121 mmol) KHF_2 (Alfa Aesar, 99+% metals basis) and 36.86 mg (0.2561 mmol) MoO_3 (in-house sample, purity verified *via* PXRD) were weighed in a glovebox and homogenized in an agate mortar. The light grey powdered mixture was subsequently transferred into a platinum capsule (99.95%, Ögussa, Vienna, Austria) and placed inside a boron nitride crucible (Henze Boron Nitride Products AG, Lauben, Germany). The reaction vessel was inserted into two separate cylindrical graphite ovens, acting as resistive heaters, and enclosed in a ZrO_2 sleeve for temperature isolation. The sample was centered and prepared for current conduction by placement of a MgO spacer and Mo platelet on either side of the cylindrical construction. Insertion into an octahedron consisting of MgO doped with 5% Cr_2O_3 completed sample preparation. To allow for quasi-hydrostatic compression of the assembly, the octahedron was surrounded by eight tungsten carbide cubes with truncated corners (Hawedia, Marklkofen, Germany) as well as six steel anvils and placed into the cylindrical cavity of the Walker-type module. With this geometric setup, the uniaxial pressure acting on the Walker-type module can be distributed equally among the eight different faces of the octahedron. Additional information regarding various assemblies and experimental setups can be retrieved from literature.[50–53]

Upon completion of the experimental setup, the pressure acting on the assembly was increased to 3.0 GPa within 80 min followed by a rise in temperature to 800 °C in 10 min. Pressure and temperature were held constant for an additional 20 min before the sample was cooled back down to 200 °C in 60 min. Finally, the reaction was quenched to room temperature. Depressurization back to atmospheric pressure was achieved within 900 min. Upon recovery of the platinum capsule and separation from other assembly materials, the product was extracted under argon atmosphere to reveal a polycrystalline sample with a slight green tint (see Fig. 8). As only larger particles exhibit a green color, the sample appears light grey after homogenization.

Powder X-ray diffraction

A powder diffractogram of HP-$K_2MoO_2F_4$ was recorded on a STOE STADI P powder diffractometer (STOE & CIE GmbH, Darmstadt, Germany) in transmission geometry. The device was operated in Debye–Scherrer mode with Ge(111)-monochromatized MoKα_1 radiation (λ = 70.93 pm) across a 2θ range of 2.0–42.0° with a step size of 0.015°. Prior to removal from the glovebox, a sample was homogenized and sealed inside a soda-lime glass capillary to allow for a measurement under ambient conditions without the interference of oxygen or air moisture. Diffracted radiation was recorded on a DECTRIS MYTHEN 1 K microstrip detector system. Subsequent Rietveld analysis was performed using the software package Diffrac^{plus} Topas 4.2 (Bruker AXS, Karlsruhe, Germany).[54]

Single-crystal X-ray diffraction

A sample of HP-$K_2MoO_2F_4$ stored under argon atmosphere was transferred onto a microscope slide and covered with perfluoropolyalkylether to allow for the selection of a suitable single crystal under a polarization microscope outside of the glovebox. The selected crystal was mounted onto a Bruker D8 Quest single-crystal diffractometer (Bruker, Billerica, USA) for measurement at an ambient temperature of 301(2) K. MoKα radiation (λ = 71.073 pm) was generated by monochromatization of radiation from an Incoatec IμS Microfocus X-ray tube (Incoatec, Geesthacht, Germany) and diffracted onto a Photon III C14 detector system.

The data was collected and monitored with the program Apex v2021.4-0.[55] Integration, data reduction and unit cell refinement were carried out in Saint-V 8.40B.[56] A multi-scan

absorption correction provided by Sadabs-2016/2[57] was applied to the intensity data. Space groups *C*2 (no. 5), *Cm* (no. 8), and *C*2/*m* (no. 12) were considered for structure solution based on extinction conditions, with *C*2/*m* (no. 12) being found to be correct. The structure was solved using Shelxtl-2018/2[58] in Olex2[59] utilizing the Shelxl 2017/1[60] refinement package employing full-matrix least-squares against F^2. Twinning *via* a twofold axis about [001] was resolved by refinement of the structure as a 2-component pseudo-merohedral twin using the twin law (−1, 0, 0, 0, −1, 0, 0, 0, 1) and a batch scale factor BASF of 0.0587(11). The presence of higher space group symmetry was ruled out by an Addsym[61,62] check in Platon.[63] Standardization of the crystal structure data was performed using the subroutine Structure Tidy.[64] Visual representations of the crystal structure were created with Diamond 4.6.8.[65]

Infrared spectroscopy

Infrared measurements were carried out on a Bruker Alpha II FT-IR spectrometer under Ar atmosphere to prevent further reaction of HP-$K_2MoO_2F_4$ with air moisture. A small amount of the product mixture was ground up together with double the amount of KBr and pressed to a transparent pellet using an apparatus capable of enacting a pressure of ≈2 tons onto the sample. The measurement was performed at room temperature across a range of 400–4000 cm^{-1} with a resolution of 2 cm^{-1}. A background correction resulting from the measurement of pure KBr was applied to the obtained sample data. The proprietary software Opus version 8.2 by Bruker was used for data handling.

Conflicts of interest

The authors declare no conflict of interest regarding this article.

Acknowledgements

The authors would like to thank Assoc.-Prof. Dr Gunter Heymann for the collection of the single-crystal data and Markus Rödl for his help with the infrared measurement.

References

1 M. Leblanc, V. Maisonneuve and A. Tressaud, *Chem. Rev.*, 2015, **115**, 1191–1254.
2 Y. Tsujimoto, K. Yamaura and E. Takayama-Muromachi, *Appl. Sci.*, 2012, **2**, 206–219.
3 P. P. Fedorov, A. A. Luginina and A. I. Popov, *J. Fluorine Chem.*, 2015, **172**, 22–50.
4 S. Bai, D. Wang, H. Liu and Y. Wang, *Inorg. Chem. Front.*, 2021, **8**, 1637–1654.
5 S. Adachi, *ECS J. Solid State Sci. Technol.*, 2019, **8**, R183–R196.
6 R. J. Clément, Z. Lun and G. Ceder, *Energy Environ. Sci.*, 2020, **13**, 345–373.
7 Da Deng, *ChemNanoMat*, 2017, **3**, 146–159.
8 S. Tang, Y. Liu, H. Li, Q. Zhou, K. Wang, H. Tang and Z. Wang, *J. Lumin.*, 2020, **224**, 117291.
9 M. Hu, Z. Liu, Y. Xia, G. Zhang, Y. Fang, Y. Liu, G. Zhao and J. Hou, *J. Mater. Sci.: Mater. Electron.*, 2020, **31**, 4535–4541.
10 T. Hu, H. Lin, Y. Cheng, Q. Huang, J. Xu, Y. Gao, J. Wang and Y. Wang, *J. Mater. Chem. C*, 2017, **5**, 10524–10532.
11 P. Cai, L. Qin, C. Chen, J. Wang and H. J. Seo, *Dalton Trans.*, 2017, **46**, 14331–14340.
12 Q. Qu, K. Chen, Y. Zhou, J. Li and H. Ji, *J. Mater. Chem. C*, 2023, **11**, 12658–12666.
13 Y. Zhou, H. Ming, S. Zhang, T. Deng, E. Song and Q. Zhang, *Chem. Eng. J.*, 2021, **415**, 128974.
14 J. Wu, B. Wang, Z. Liu, K. Zhang, X. Li, J. Huang, P. Liu and Q. Zeng, *Dalton Trans.*, 2021, **50**, 11189–11196.
15 S. He, L. Yao, W. Cai, Di Wu, J. Peng and X. Ye, *Dalton Trans.*, 2020, **49**, 11290–11299.
16 G. Jander and B. Fiedler, *Z. Anorg. Allg. Chem.*, 1961, **308**, 155–158.
17 G. Z. Pinsker and V. G. Kuznetsov, *Kristallografiya*, 1968, **13**, 74–79.
18 O. Schmitz-Dumont and P. Opgenhoff, *Z. Anorg. Allg. Chem.*, 1954, **275**, 21–31.
19 D. Grandjean and R. Weiss, *Bull. Soc. Chim. Fr.*, 1967, **8**, 3049–3054.
20 D. Grandjean and R. Weiss, *Bull. Soc. Chim. Fr.*, 1967, **8**, 3044–3049.
21 D. Grandjean and R. Weiss, *Bull. Soc. Chim. Fr.*, 1967, **8**, 3040–3043.
22 D. Grandjean and R. Weiss, *C. R. Seances Acad. Sci., Ser. C*, 1966, **26**, 1864–1865.
23 Z. H. Jie, A. Garcia, F. Guillen, J. P. Chaminade and C. Fouassier, *Eur. J. Solid State Inorg. Chem.*, 1993, **30**, 773–787.
24 M. F. Hazenkamp, E. H. Voogt and G. Blasse, *J. Solid State Chem.*, 1992, **101**, 26–31.
25 I. D. Brown, *The Chemical Bond in Inorganic Chemistry: The Bond Valence Model*, Oxford University Press, Oxford, United Kingdom, 2nd edn, 2016.
26 I. D. Brown, *Chem. Rev.*, 2009, **109**, 6858–6919.
27 I. D. Brown, *Chem. Soc. Rev.*, 1978, **7**, 359–376.
28 J.-G. Eon and M. Nespolo, *Acta Crystallogr., Sect. B: Struct. Sci., Cryst. Eng. Mater.*, 2015, **71**, 34–47.
29 M. Nespolo, G. Ferraris and H. Ohashi, *Acta Crystallogr., Sect. B: Struct. Sci.*, 1999, **55**, 902–916.
30 R. Hoppe, S. Voigt, H. Glaum, J. Kissel, H. P. Müller and K. Bernet, *J. Less-Common Met.*, 1989, **156**, 105–122.
31 R. Hoppe, *Z. Kristallogr. – Cryst. Mater.*, 1979, **150**, 23–52.
32 L. Pauling, *The Nature of the Chemical Bond: An Introduction to Modern Structural Chemistry*, Cornell University Press, Ithaca, New York, 3rd edn, 1960.
33 L. Pauling, *J. Am. Chem. Soc.*, 1929, **51**, 1010–1026.
34 L. Pauling, *J. Am. Chem. Soc.*, 1947, **69**, 542–553.

35 G. Donnay and R. Allmann, *Am. Mineral.*, 1970, **55**(5–6), 1003–1015.
36 I. D. Brown, *J. Solid State Chem.*, 1974, **11**, 214–233.
37 I. D. Brown and R. D. Shannon, *Acta Crystallogr., Sect. A: Found. Adv.*, 1973, **29**, 266–282.
38 N. E. Brese and M. O'Keeffe, *Crystallogr., Sect. B: Struct. Sci.*, 1991, **47**, 192–197.
39 I. D. Brown and D. Altermatt, *Crystallogr., Sect. B: Struct. Sci.*, 1985, **41**, 244–247.
40 M. Nespolo, *Acta Crystallogr., Sect. B: Struct. Sci., Cryst. Eng. Mater.*, 2016, **72**, 51–66.
41 R. Hoppe, *Z. Naturforsch., A: Phys. Sci.*, 1995, **50**, 555–567.
42 R. Hoppe, *Angew. Chem., Int. Ed. Engl.*, 1981, **20**, 63–87.
43 R. Hoppe, *Angew. Chem., Int. Ed. Engl.*, 1970, **9**, 25–34.
44 R. Hoppe, *Angew. Chem., Int. Ed. Engl.*, 1966, **5**, 95–106.
45 R. Hübenthal, *MAPLE v4*, University of Gießen, Germany, 1993.
46 C. E. Weir and G. J. Piermarini, *J. Res. Natl. Bur. Stand., Sect. A*, 1964, **68A**, 105–111.
47 H. Shorafa, H. Ficicioglu, F. Tamadon, F. Girgsdies and K. Seppelt, *Inorg. Chem.*, 2010, **49**, 4263–4267.
48 F. Ding, K. J. Griffith, C. P. Koçer, R. J. Saballos, Y. Wang, C. Zhang, M. L. Nisbet, A. J. Morris, J. M. Rondinelli and K. R. Poeppelmeier, *J. Am. Chem. Soc.*, 2020, **142**, 12288–12298.
49 R. E. Stene, B. Scheibe, A. J. Karttunen, W. Petry and F. Kraus, *Eur. J. Inorg. Chem.*, 2019, **32**, 3672–3682.
50 H. Huppertz, G. Heymann, U. Schwarz and M. R. Schwarz, in *Handbook of Solid State Chemistry*, ed. R. Dronskowski, S. Kikkawa and A. Stein, John Wiley and Sons Ltd, New Jersey, USA, 2017, 2, pp. 23–48.
51 H. Huppertz, *Z. Kristallogr. – Cryst. Mater.*, 2004, **219**, 330–338.
52 D. Walker, *Am. Mineral.*, 1991, **76**, 1092–1100.
53 D. Walker, M. A. Carpenter and C. M. Hitch, *Am. Mineral.*, 1990, **75**, 1020–1028.
54 A. A. Coelho, *J. Appl. Crystallogr.*, 2018, **51**, 210–218.
55 *Apex4*, Bruker AXS Inc., Madison, Wisconsin, USA, 2021.
56 *SAINT-V (version 8.40B)*, Bruker AXS Inc., Madison, Wisconsin, USA, 2021.
57 G. M. Sheldrick, *SADABS (version 2016/2)*, University of Göttingen, Germany, 2016.
58 G. M. Sheldrick, *Acta Crystallogr., Sect. A: Found. Adv.*, 2015, **71**, 3–8.
59 O. V. Dolomanov, L. J. Bourhis, R. J. Gildea, J. A. K. Howard and H. Puschmann, *J. Appl. Crystallogr.*, 2009, **42**, 339–341.
60 G. M. Sheldrick, *Acta Crystallogr., Sect. C: Struct. Chem.*, 2015, **71**, 3–8.
61 Y. Le Page, *J. Appl. Crystallogr.*, 1988, **21**, 983–984.
62 Y. Le Page, *J. Appl. Crystallogr.*, 1987, **20**, 264–269.
63 A. L. Spek, *Acta Crystallogr., Sect. D: Biol. Crystallogr.*, 2009, **65**, 148–155.
64 L. M. Gelato and E. Parthé, *J. Appl. Crystallogr.*, 1987, **20**, 139–143.
65 H. Putz and K. Brandenburg, *Diamond - Crystal and Molecular Structure Visualization*, Crystal Impact, Bonn, Germany, 2022.